

Growing Negative Pressure in Dissolved Solutes: Raman Monitoring of Solvent-Pulling Effect

Lionel Mercury^{*1}, Kirill I. Shmulovich², Isabelle Bergonzi¹, Aurélien Canizarès³, Patrick
Simon³

¹ Institut des Sciences de la Terre d'Orléans, UMR 7327 Université d'Orléans / CNRS / BRGM, 1A rue de la Férollerie, 45071 Orléans cedex (France). lionel.mercury@univ-orleans.fr. Phone: +33 (0)238.255.398. Fax: +33 (0)238.494.476.

² Institute of Experimental Mineralogy, Russian Academy of Science, 142432 Chernogolovka (Russia).

³ CNRS, UPR3079 CEMHTI, Université d'Orléans, 1D avenue de la Recherche Scientifique, CS 90055, 45071 Orléans Cedex 2 (France).

ABSTRACT

Negative pressure in liquids is both an experimental fact and a usually-neglected state of condensed matter. Using synthetic fluid inclusions, namely closed vacuoles fabricated inside one solid host by hydrothermal processes, a Raman study was performed to examine how a superheated solvent (under negative pressure) interacts with its dissolved solutes. As a result, this contribution not only illustrates this well-known tensile state, but also displays evidence that a stretched solvent is able to pull on its dissolved solutes and put them also under a stretched state. The dielectric continuum hypothesis may lead to expect a stretching effect in solutes similar to the solvent's, but our measurements evidence a damping mechanical effect (growing with tension), most probably related to solvation shells. One practical consequence is that the (experimentally known) super-solvent properties of superheated solutions are certainly related to the change of the chemical potential of solutes which results from the damping effect. This change can determine as well a change in the thermodynamic driving force of the superheated solution towards bubble nucleation. A more complex than usual picture of the aqueous solution physical chemistry emerges from this study.

1. INTRODUCTION

Negative pressure is still nowadays a paradoxical-sounding concept, because the notion collides between gases, for which the zero pressure is an absolute limit (pressure and matter density are strictly proportional at low density), and condensed matter, the internal cohesion of which allows them to resist tensile (pulling) as pressurizing (pushing) forces (pressure, which can be also called strain, is a vectorial quantity)¹. One interest to study the tensile (or stretched) liquids is that they are metastable with respect to their vapor: there are superheated liquids. The extent of superheating for one liquid (extreme tensile strength) and its behavior in this peculiar state give insights into its anomalous properties, themselves precious to delineate its complete phase diagram. Water is particularly under scrutiny due to its huge importance in almost every processes on Earth, also due to its easiness to experience superheating, while it shares the generic features of van der Waals liquids.

The first and main objective of this study is to explore how the superheating may impact the solvent properties of the tensile water so that to make it a super-solvent. It is largely established that the liquid tension should increase the solubility of solids and gases, on theoretical²⁻³ and experimental⁴⁻⁷ grounds, with natural and industrial interesting consequences⁸⁻¹⁰, especially in green chemistry treatments¹¹⁻¹². However, the classic assumption when trying to quantify this effect is to assume that the dissolved solutes are at the same pressure as the solvent itself, viewing an aqueous solution as a continuum dielectric medium^{2-6,13}. This hypothesis has never been tested to the best of our knowledge. These super-solvent properties are accounted for through the lowering of the dielectric constant, and/or changes in the viscosity properties and gas-like diffusion rates. The present contribution is discussing how the solvent-solutes interactions may participate in causing these properties changes.

The best technique to explore the tensile forces of liquids is one of the most ancient one, the Berthelot's tube-type fluid inclusions (synthetic fluid inclusions, SFIs), with which all the major measurements of superheating were obtained^{8,14-17}. It will be the technique of choice for the

present study to produce a superheated aqueous solution owing to micro-thermometric procedure: the variation of temperature in a closed fluid-filled vacuole makes the P-T conditions to move either along a saturation line (biphasic assemblage) or along an isochoric curve (monophasic fluid). T is measured, while P is calculated using the equation of state (EoS) of the solution, along the saturation line or along the isochore, possibly extrapolated down to the tensile domain. The trapped liquid is constituted by an aqueous solution of Na_2WO_4 containing one solute with a pressure-sensitive Raman peak: the WO_4 tetrahedron has a Raman symmetric breathing mode, the wavenumber of which significantly and linearly shifts with pressure¹⁸. A spectroscopic study measured, at the same T, the frequency difference of the WO_4 wavenumber between the liquid-vapor equilibrium and the monophasic tensile state. This difference is related to the pressure felt by the solute to be compared to the pressure of the solution predicted by the EoS. The chemical potential of the solute in the superheated solution can thus be evaluated, with respect to the chemical potential of the stretched solvent.

A second objective of the present study is to clarify the role (or the absence of role) of the amount of dissolved solutes on the way the superheated liquids behave. An overlooked aspect when using the SFIs is about the exact composition of the liquids under study. It is usually considered that the liquid trapped inside the SFIs is the one supplied initially during the fabrication procedure, and therefore possibly pure water. However, during the hydrothermal synthesis, the conditions can go up to several kbar and hundreds of degrees Celsius during weeks, conditions at which the quartz solubility drastically increases (quartz solubility is around 0.1 mol/kgw at P-T synthesis conditions¹⁹, and 10^{-4} mol/kgw at room temperature), deviating the initial composition of the trapped liquid by a certain shift¹⁵. According to a detailed and systematic micro-thermometric study⁸, there is a close connection between the composition and the extreme tensile strength, what was then referred to a surface tension effect. Our present ability to distinguish between solute pressure and solution pressure paves the way to refine our understanding of these compositional effects of the fracture of liquids.

2. MATERIALS AND METHODS

2.1 Synthetic Fluid Inclusions (SFIs)

SFIs are micro-cavities in a solid crystal (here, quartz) hosting an occluded liquid, synthesized in internally-heated pressure vessels⁸. The chosen solution is a 2.5M (M for mol/kgw molal unit; 42.3%wt) solution of Na_2WO_4 (crystal solubility is 74.2 %wt at 25°C²⁰), initially at liquid-vapor saturated conditions. Actually, the Raman symmetric breathing mode wavenumber of the WO_4 tetrahedron (near 930 cm^{-1}) is highly sensitive to the local pressure (see section 2.3). Additionally, the wavenumber of this mode is far from those of quartz (216 and 465 cm^{-1}) and then the tungstate mode wavenumber can be safely isolated.

After thermal cracking, the synthetic quartz pieces were put in Pt capsules together with the target solution (100 μL) and amorphous silica (10 mg). 30 days at 500 MPa and 450°C (density about 1022 kg/m^3) made the liquid to be trapped in the cracks as they seal during the run, building series of inclusions throughout the sample (Fig. 1). After double-side polishing and direct optical observation (quartz is transparent in the visible spectrum), one FI (Fig. 1) was selected for the readiness of observation, and closeness to sample surface ($\leq 10 \mu\text{m}$). It was 18 $\mu\text{m} \times 8 \mu\text{m}$ in size, shaped pretty close to a negative quartz crystal, indicative of equilibrium growth and recrystallization conditions.

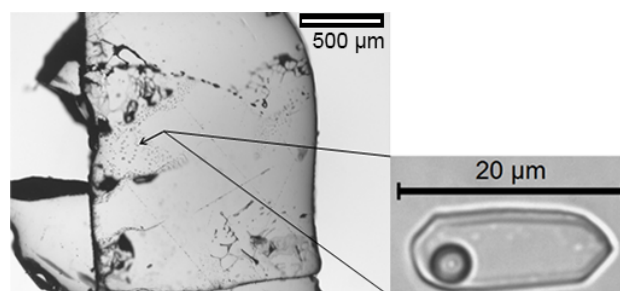


Figure 1. Left: 5X photograph of the synthetic quartz fragment containing fluid inclusions. Right: 100X magnified image of the selected inclusion at room conditions (L+V assemblage in the vacuole), containing Na_2WO_4 42.3%wt.

2.2 Micro-Thermometric Procedure

As SFIs are closed systems, any thermal changes displace the trapped liquid in its P-T space according to the rules of phase diagram, in its stable or metastable behaviors^{7-8,21}. The thermal changes in the inclusion are done putting the quartz fragment on a Linkam heating-cooling stage (THMS 600), precisely controlled ($\pm 0.1^\circ\text{C}$). To avoid thermal gradients related to the thickness of the fragment, capping the sample with a silver cover is very efficient^{8,22}.

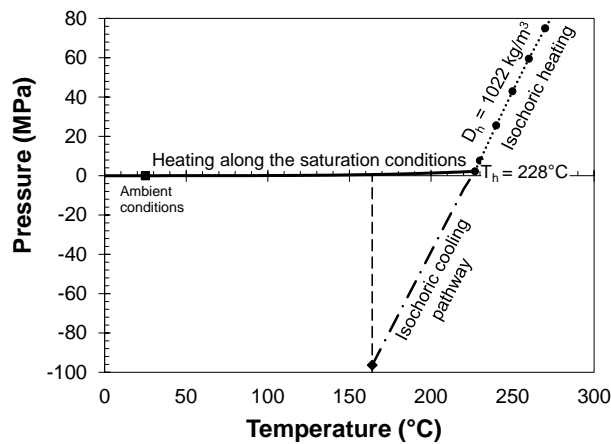


Figure 2. Phase diagram illustrating the classic micro-thermometric path (see text), from the ambient conditions to the homogenization (Th) and nucleation (Tn) temperatures.

The micro-thermometry technique (illustrated in Fig. 2) practically consists of the progressive heating of the sample from room temperature (RT), while the inclusion contains the biphasic liquid+vapour assemblage (L+V) (heating bold line, Fig. 2). At a particular T, the bubble, the size of which was diminishing along the LV saturation curve, disappears: there is no more vapour and the inclusion is said to be homogenized, at the so-called homogenization temperature (Th point, Fig. 2). A classic difficulty about the Th determination is that, close to the temperature, the bubble is not really visible, but a sort of shadow having Brownian motion is distinguishable: Th is measured when it disappears. It needs a careful process to be repeated to confirm the exact value. One noticeable point is that Th fixes the trapped liquid density: as long as it remains constant, the inclusion repeatedly behaves as an isochoric body. Throughout this study, Th never changes, meaning that all the thermal cycles did not modify at all the density of the SFI.

Further heating above T_h makes (P,T) to increase inside the inclusion along the isochore (isochoric heating dotted line, Fig. 2): trapped liquid is pressing upon the inclusion walls. Then, a progressive cooling of the sample along an isochoric path (dashed line, Fig. 2) put the trapped liquid into a growing tension. The temperature of the immediate bubble appearance is called the instantaneous nucleation temperature, noted T_n and is always lower than T_h . T_n characterizes the extreme tensile strength of the probed inclusion. Another suitable angle of view is to state that the lifetime of the metastable state diminishes when going deeper in the tensile domain, to reach 0 at T_n . In-between T_h and T_n , is the growing tension range of the inclusion, along which the liquid is less stable than the L+V assemblage (why it is called superheated), prevented from taking place during a certain lifetime, due to the energy cost of the liquid-air interfaces fabrication^{6,23-24}.

2.3 Raman Setup and Procedure

In situ Raman spectroscopy can be used to record the temperature/pressure shift due to the phonon anharmonicity of a Raman-active vibration mode²⁵. This phonon anharmonicity is responsible for the frequency shift of vibration modes upon external strains such as temperature or hydrostatic pressure. A previous study¹⁸ studied the shift under pressure of the wavenumber of the Raman symmetric breathing mode of different dissolved compounds (anthracene, perchlorate, tungstate) and concluded that the tungstate ion was the only one suited to record the isothermal pressure dependence, with a linear dv/dP .

The WO_4 wavenumber was recorded in the SFI of choice along the whole microthermometric path, namely from positive pressure (biphasic state) to tension (monophasic state, below T_h). The wavenumber difference at the same temperature between the two states is interpreted in terms of local pressure of the solute, owing to a calibrated wavenumber-pressure calibration. Therefore, the Raman response is obtained at constant geometry, optical configuration, and temperature except the varying in-SFI liquid pressure (the only changing parameter), what gives very strong grounds to use the Raman shifts as a pressure probe.

A dv/dP calibration of the WO_4 Raman mode is available in the literature, performed at room temperature (RT) with a 1M solution¹⁸, resulting in a $8.2 \times 10^{-3} \text{ cm}^{-1}/\text{MPa}$ slope. A second calibration has been done at 162°C (T_n , see below) with a 2.5M solution, to check for a possible thermal / concentration effect on the calibration (Fig. 3). A Renishaw RA100 portable spectrometer was mounted onto the high T-P cell developed at the Institut Néel (CNRS Grenoble, France), including an inner glassy-carbon cell heated by electrical resistances and inserted in a stainless steel vessel pressurized with helium²⁶. The high pressure vessel size is $242 \times 150 \text{ mm}$, and it is equipped with water-cooling jacket and windows for laser passage. The two calibration datasets match very well to each other (Fig. 3), demonstrating that the 1M to 2.5M Na_2WO_4 change and the 23°C to 162°C difference do not significantly affect the linear trend with pressure: the dv/dP retained for this study is: $dv/dP = 8.2 \times 10^{-3} (\pm 3 \times 10^{-4}) \text{ cm}^{-1}/\text{MPa}$. This linear dependency means that the phonon anharmonicity of the Raman-active vibration mode depends very little on the higher-order terms of the function: though involved, they certainly are of very small magnitude²⁵.

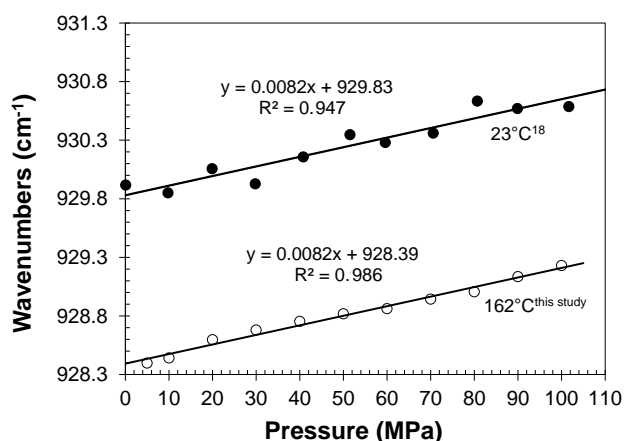


Figure 3. Raman WO_4 mode wavenumber recorded as a function of pressure at constant temperature: 162°C (open points, this study) and 23°C ¹⁸ (black points). The slope is T-independent.

The spectroscopic measurements on the SFI were performed on a Renishaw Invia Reflex spectrometer, using the 633nm excitation line of a He-Ne laser (less than 10mW on the sample). The grating was 1800 grooves/mm, giving a wavenumber step between two

adjacent pixels of the CCD equal to 0.97 cm^{-1} . Each measurement was done after a wavenumber calibration procedure of the spectrometer on its internal silicon reference sample (520.5 cm^{-1}), without moving the quartz sample, which ensures the calibration state and promotes the highest possible reproducibility. The microscope (DM2500 Leica) objective compatible with this configuration was a Leica 50X long front distance (NA=0.50). Each Raman spectrum was obtained with an accumulation time of 120s. Spectra were treated with the Renishaw Wire 3 software. The sensitivity and the stability of such recent Raman spectrometer make us able to extract unambiguously even very small features, which can be completely masked by noise and fluctuations in a routine experiment.

Raman measurements were performed on the selected SFI (Fig. 1 right) from $T_h+29^\circ\text{C}$ (257°C) down to $T_n+2^\circ\text{C}$ (164°C), namely from overpressure to tensile situation. At each temperature, two measurements have been done, one when heating from RT and then with a biphasic L+V vacuole, the other after crossing T_h , and then with a monophasic only-liquid filled vacuole. A 2°C thermal step was used, and the cooling down sequence carried out at slow rate ($2^\circ\text{C}/\text{min}$) to avoid any temperature overshoot and to insure rapid thermal equilibrium after arriving at each set point. In addition, a waiting time of 2 minutes was systematically respected before recording any spectrum. This time was used to check and adjust the position of laser focusing inside the inclusion: horizontally, and vertically, by measuring the distance between the surface (where the position of laser focusing can be measured with accuracy better than one μm) and the analysis point inside inclusion.

2.4 Raman Data Processing

The Raman spectra was not baseline-corrected but directly fitted with a Gauss-Lorentz (G/L hereafter) profile, to involve even the tiniest distortions into the analysis. Very small differences between mono- and biphasic conditions can thus be probed, since the spectra were acquired with strictly identical conditions (optical configuration, temperature), apart the pressure inside the inclusion.

The fit gave three interesting parameters per spectrum: position, width and shape (G/L ratio). All fits were performed with the same set of starting values, to favour the significance and comparability of the calculated final values. Widths and shapes are slightly temperature dependent or constant within experimental accuracy, but do not exhibit any difference between monophasic and biphasic regimes (Fig. 4); they will not be more discussed here. Much more interesting is the position of the line center, which is the focus of the present contribution.

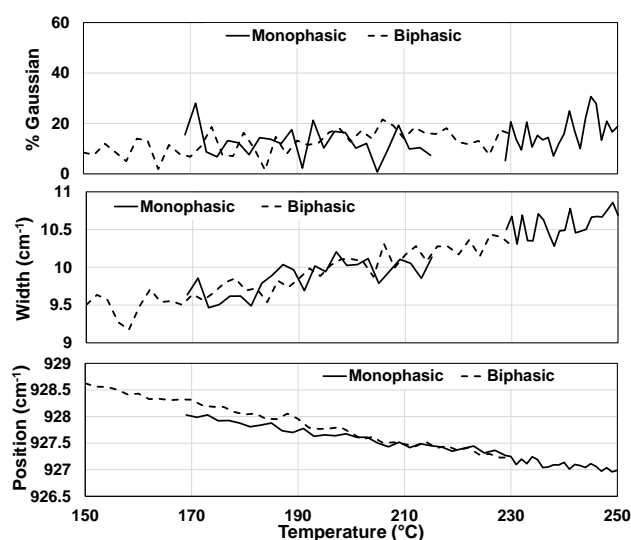


Figure 4. Temperature dependence of linewidths, shapes (Gaussian/Lorentzian ratio), and wavenumber of the line center. Only this latter differs from mono- to biphasic states.

No Bose-Einstein (BE) thermal correction was done²⁷, since Raman shifts are compared at identical temperatures in two different pressure conditions (monophasic and biphasic regimes). Moreover this correction would be practically negligible since the linewidth vs. line position ratio is very low.

3. RESULTS

3.1 In-SFI Superheating

The melting temperature of the studied inclusion is -18.1°C , corresponding to an analogous 4.6M NaCl load in the inclusion, reasonably consistent with the divalent 2.5M Na_2WO_4 . At such high initial salinity, it seems that the hydrothermal synthesis does not change much the

total concentration. Hereafter, as no Na_2WO_4 EoS is available, we will assume that a 5M NaCl solution (for which EoS are available) stands for our tungstate solution. This hypothesis is especially valuable for the LV saturation curve, because saturation pressures are not greatly influenced by the exact nature of the solutes²⁸.

The thermal cycle performed on the SFI followed the saturation line from RT (20°C, 2.10^{-3} MPa, $D = 1169 \text{ kg/m}^3$) to 162°C (0.55 MPa, $D = 1078 \text{ kg/m}^3$), and then to Th (228°C, 2.28 MPa, $D_h = 1022 \text{ kg/m}^3$). One important feature is that the Th value never changed through the three years of this study, across one hundred or more of thermal cycles, and several full runs of Raman measurements. This means that the density of the trapped liquid kept constant throughout, despite regularly undergoing compression (isochoric heating above Th) as tension (isochoric cooling below Th). This Th constancy means that any mechanical deformation, sometimes observed with inclusions^{15,17}, can be discarded and strongly supports our isochoric hypothesis.

Further cooling the sample leads to vapor phase nucleation, not at Th (228°C) but at Tn (162°C) < Th. The hysteresis $\Delta T = T_h - T_n$ characterizes the penetration of the system into the metastable region of the stretched liquid: $\Delta T = 65^\circ\text{C}$, a mean value with respect to the already observed¹⁰ 110°C (H_2O) or 135°C (CsCl). To transform this T hysteresis into a lower-than-saturation pressure, we need to assume that the cooling follows an isochoric path, and that the isochoric curve under tension is the linear extrapolation of its positive pressure counterpart (Fig. 2). As noted above, the saturation line and the isochoric calculations are performed according to the very recent EoS from Mao and Duan²⁹, at 5M NaCl, the monovalent equivalent of Na_2WO_4 , consistent with the Tm measurement.

3.2 Raman Datasets

The WO_4 mode wavenumbers were recorded from RT up to 257°C (Fig. 5), and lines up as a straight line from 150°C to 257°C, deviating from this linear alignment below 150°C. Practically, the linear part corresponds to a temperature-independent vibration anharmonicity, while the slightly curved part is related to some change in it. When extended

down to RT, the Raman symmetric mode of WO_4 stands at 931.25 cm^{-1} , consistent with 931.1 cm^{-1} in the literature³⁰, and the corresponding accuracy of the internal calibration of the spectrometers.

At $T > T_h$, the thermal cycle was reversed to a cooling stage, and the Raman measurements were performed under monophasic superheated/stretched conditions, down to the T_n at which the bubble re-appears by cavitation. The measured wavenumbers systematically align along a new straight line according to a smaller slope than the biphasic linear dataset. More than thirty measurements were performed, in both monophasic and biphasic regimes, and so the accuracy of the straight lines drawn through all these points (linear regression fit) are much better than the precision of each measurement point taken individually.

The absence of correction (neither baseline subtraction nor Bose-Einstein factor) of the raw experimental data in the linear ($164^\circ\text{-}257^\circ\text{C}$) range gives support to a direct interpretation of the increasing Raman deviation in terms of pressure shift between the two in-SFI liquid states.

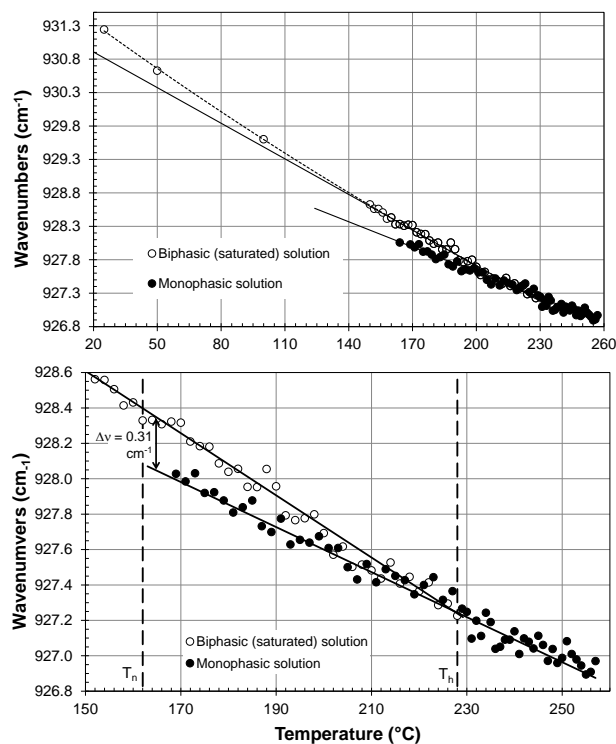


Figure 5. Top. Raman WO_4^{2-} mode wavenumber measured over the whole experimental range, evidencing a linear and then slightly curved vibration. Bottom. T range over which T-

independent vibration is observed. Two linear trends arise with the data from the monophasic solution deviating from those from the biphasic Raman, more and more with decreasing T.

The superposed spectra at two different T (Fig. 6) illustrate that the difference between the biphasic and monophasic-based spectra is very small: the spectrum taken on the tensile metastable solution lies at a tiny lower wavenumber than the one characteristic of the equilibrium stable situation. Considering the close proximity between the datasets, we carried out several times the whole measurements, trying to improve each time the thermal stability of the experimental room. The gap between the biphasic and monophasic datasets was systematically retrieved and confirmed: the two straight lines systematically have slightly different slopes, meaning the gap is proportional to something varying linearly in the inclusion undergoing the two states. The line center exhibits a small but unambiguous gap, and the linear correlation of the measured points is evident. The best linear fit $\nu_{\text{WO}_4} = A + B.T$ (T in °C) quantifies the difference:

$$\nu_{\text{WO}_4} = 930.1 (\pm 0.06) - 0.0127 (\pm 3 \cdot 10^{-4}).T, \text{ for the monophasic regime,}$$

$$\text{and } \nu_{\text{WO}_4} = 931.2 (\pm 0.07) - 0.0176 (\pm 4 \cdot 10^{-4}).T, \text{ for the biphasic one.}$$

The uncertainty on the intercept A and the slope B was calculated by the linear regression routine. In the fit, the two sets of data were calculated simultaneously, and one strain was given: the two trend lines had to cross at T_h , at which there is no more difference between the two sets, physically.

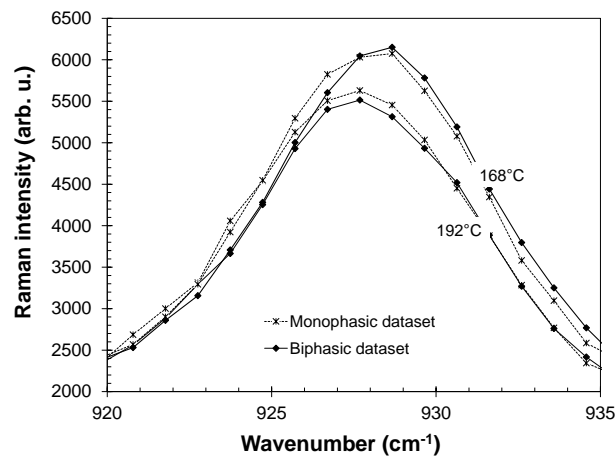


Figure 6. Typical spectra of the WO_4^{2-} line at 192°C and 168°C in the metastable and equilibrium states. The points correspond to measurements on each CCD pixel. The raw curves (displayed) were fitted to extract the line features (width, position, shape; see text).

The maximum difference (0.31 cm^{-1}) is actually noticeably lower than the spectral resolution (*i.e.*, the ability to separate two lines of similar intensity: about $3\text{-}4 \text{ cm}^{-1}$) and also lower than the step between two adjacent CCD pixels (0.97 cm^{-1}). What is essential here is the stability of the spectrometer, *i.e.*, its ability to give the same result to successive measurements done in the same conditions, mainly owing to the thermal stability of the spectrometer room (better than $\pm 0.5^\circ\text{C}$), which improves the internal calibration of the spectrometer. This calibration with the internal silicon reference of the spectrometer was always performed exactly in the same way, owing to an automatized procedure, and on the same point of the sample. As a result, the wavenumber stability over the measurement time (20 hours typically) is estimated to be better than 0.1 cm^{-1} , including the uncertainty due to the fitting process. The difference of 0.31 cm^{-1} (Fig. 5 bottom) is calculated between the positions of the two mono- and biphasic trend lines ($dv_T = v_{\text{biphasic},T} - v_{\text{monophasic},T}$), and not between two measured points, giving a more accurate value than the experimental points themselves. Precisely, the error bar on the measured dv , has got a twice better precision than the points correlation of the two straight lines: $dv = 0.31 \text{ cm}^{-1} \pm 0.05 \text{ cm}^{-1}$ at 164°C .

3.3 Solute Raman-Based Pressure

The straightforward conclusion is to assign the linearly-increasing Raman shift to the tensile effect that linearly grows in the SFI upon cooling (Fig. 7). Using the calibration reported above, which is directly extrapolated in the tensile domain, the tension felt by the anion at 164°C is equal to -37 MPa . This calculation can be decomposed as follows: the Δv measured at 164°C is 0.31 cm^{-1} , that turns into $\Delta P = -37.8 \text{ MPa}$ (ratio $0.31 \text{ cm}^{-1}/0.0082 \text{ cm}^{-1}/\text{MPa}$). The saturation pressure (of NaCl 5M) at 164°C is equal to $+0.6 \text{ MPa}$, so that the net tension of the solute is equal to: $P = -37 \text{ MPa} \pm 7 \text{ MPa}$. The uncertainty on this value results mainly

from the uncertainty on the dv ($\pm 0.05 \text{ cm}^{-1}$) value between biphasic and monophasic lines, and on a lesser extent from the $\nu - P$ calibration (Fig. 3).

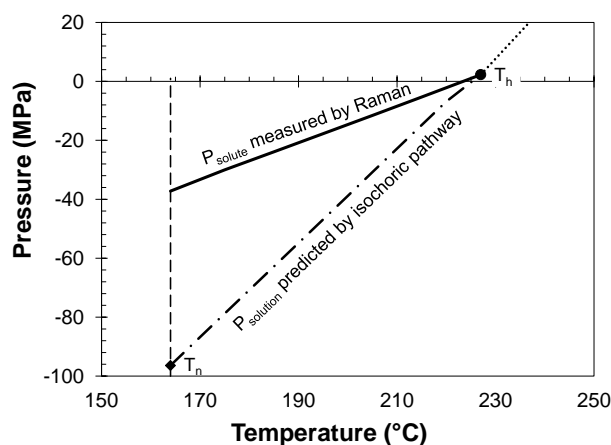


Figure 7. Comparison between the solution pressure calculated by the 5M NaCl equivalent EoS extrapolation inside the tensile domain, and the WO_4 solute pressure as measured by its Raman symmetric mode wavenumber.

Therefore, this measurement demonstrates that the tension in the solvent is transmitted to the ion which experiences a stretched state. An interesting aspect is exhibited by the monophasic straight line without any anomaly at T_h (Fig. 5 bottom). It crosses from metastable to stable (or the reverse) conditions continuously, then evidencing a continuity in the microscopic parameters (anharmonicity) governing the Raman mode wavenumber. This monotonic behavior indicates that the pressure drop around the ion is only related to the traction from the surrounding solvent (mechanical effect), and not to a change in the dielectric screening (electrical effect) under tension, that would affect the anharmonicity parameters. It explains why the screening is increasing under growing tension (restoring force effect).

3.4 Liquid EoS-Based Pressure

Proceeding a little bit further, we can also evaluate the tension in the liquid with an equation of state (EoS) along $T < T_h$. The principle is to calculate the liquid density D_h at T_h , and then, calculate, through the (D_h, T) couple, the existing pressure in the isochorically-cooled liquid.

Old and recent results^{8,14-17,31} strongly establish this extrapolative ability, despite it seems likely that the scope should be limited, around -100 MPa for liquid water probably^{8,17,32}.

The NaCl EoS used presently²⁹ has been already tested against negative pressures^{8,10}. We used it to calculate the (Dh,Ph) values from the experimental Th 228°C: Dh = 1022 kg/m³. The corresponding isochoric curve can be calculated and gives us the dP/dT slope of the isochore. Assuming a straight line extension into the superheated domain²², the pressure along the isochoric cooling procedure can be deduced:

$$P(\text{MPa}) = \left(\frac{dP}{dT} \right)_{\text{MPa}/^{\circ}\text{C}} \times T(^{\circ}\text{C}) + b$$

This procedure results in a dP/dT slope equal to 15.8 MPa/°C and a tension at 164°C amounting to -96.4 MPa (Fig. 7). To try assessing the uncertainty related to the empirical EoS, we performed the same calculation with another classic Eos, from Bodnar³³, which gave: dP/dT = 17.2 MPa/°C, and a tension at 164°C equal to -107.5 MPa. However, the uncertainty of the calculations is significantly lower than the gap between the Raman-based pressure (-37 MPa) and the micro-thermometric-based one (-96 to -107 MPa).

4. DISCUSSION

This discrepancy between the tension felt by the solution and the local tension undergone by the solute molecules is probably related to the damping effect played by the solvation shell around the ion which buffers the liquid tension. The electrostriction pressure living inside the first hydration shell can be calculated by thermodynamics and electrostatics from the Onsager local field model³⁴⁻³⁶: water molecules within the first hydration shell of Na⁺ undergo 110 MPa, the ones of Cl⁻ is at 30 MPa, while we did not find data for WO₄²⁻ or even SO₄²⁻. Therefore, a weakened tension in the anion than in the solvent should be expected. As a consequence, we demonstrate that an aqueous solution is a dielectric continuum more and more different under growing tension than the reference state situation, on both the solvent and the solutes viewpoints.

This mechanical solvent-driven traction counteracted by electrostriction (by a mechanical screening) deviates the solvation water from the solvent water. Logically this effect may acquire a larger influence on the behavior of the global solution with its concentration, due to the increasing fraction of solvation water vs. solvent water. It offers an alternative explanation of the stronger superheating behavior of certain aqueous solutions: NaCl, CaCl₂ and CsCl display increasing superheating extent with respect to dilute water⁸. This is interestingly in the increasing order of the hydration number and shell radius in the first solvation shell: from 4 H₂O molecules and 240 pm (pm for picometer) for Na⁺, to 6 and 240 pm for Ca²⁺, up to 8 and 320 pm for Cs⁺, while the Cl⁻ anion has 6 molecules and a shell radius of 310 pm³⁷. Twice more water molecules are part of the first hydration shell with CsCl solutions than with the NaCl ones: assuming this solvation shell is the locus of the damping effect proposed in this study, it means that with CsCl, twice more water molecules undergo a tension lower than the free water molecules. This decreased tension would decrease the thermodynamic driving force towards nucleation, especially at high concentration when very few free water molecules remain in the solution.

From a different viewpoint, it can be observed that the solvation thermodynamics is certainly influenced by the stretched state through the V.dP term in the calculation of the chemical potential of hydrated solutes with pressure³⁸. As hydrated Na⁺ and Ca²⁺ have negative volumes (apparent volume at infinite dilution) at ambient pressure³⁹, which becomes more and more negative under tension³, the chemical potential becomes more positive with tension: tension makes the hydrated Na⁺ and Ca²⁺ less stable. Meanwhile, Cs⁺ ion has positive volume from ambient conditions down to -90 MPa, and as such, an increasing tension means a better stability for the hydrated Cs⁺, with the reverse trend beyond -90 MPa. This diversity in the behavior of the dissolved solutes in stretched solution is forcibly linked to the solubility properties of the corresponding salt in such solution. The damping effect would lead to an increased solubility of salts in a superheated solution, each time the corresponding solute has a negative volume of hydration, for instance, NaCl and CaCl₂ superheated solutions. The reverse is true for the situation in which the solutes have a positive volume of

hydration, as is Cs in a certain range of tension. It is noticeable that water molecules do not experience the same solvation pressure in the first hydration shell, which is a good image of a varying damping effect. Water molecules within the first hydration shell of Cs^+ undergo 30 MPa, the ones of Na^+ is at 110 MPa, and solvation water of Ca^{2+} is at 3.2 GPa. These values have to be combined with the hydration number to evaluate the damping effect, and therefore any consequences (solubility, nucleation or whatever) of the decreased tension around solute. It is interesting to notice that the solvation pressure is smaller for the CsCl while it is more prone to superheating. Two facts are worth to be outlined. First, CsCl has a three times lesser solvation pressure but a twice larger hydration number, and the damping effect is certainly a combination of the two. Second, the change in the thermodynamic driving force comes into play with the usually considered surface tension effect which acts by enhancing the nucleation barrier.

As a result, the mechanical screening by the solvation shells cannot be expected to follow a simple law, and a complex picture for the physical chemistry of aqueous solutions under tension arises. It requires to consider separately (but not independently) the solids, solutes and solvent pressures. Interestingly, the behavior of solutions under positive pressure should also consider such effects.

5. CONCLUSION

As a conclusion, successful measurements of a growing tension in one aqueous solution have been performed by Raman scattering owing to: (i) original samples having the liquid closed inside a solid matrix in a vacuole at constant volume according to conditions. (ii) one very stable spectrometer with a very reliable reproducibility. (iii) a very precise thermal regulation at the room scale. These results demonstrate the complexity of a tensile solution with respect to the pure liquid: solvation shells makes the pressure to vary locally from the solvent pressure around. The tension field in the solution is not continuous and the water dielectric continuum is therefore deeply disturbed by the presence of solutes. The behavior of

the water solvent, for instance with respect to its bubble nucleation barrier, is changed. As a rule of thumb, only five water molecules remains free of solute interactions in a 2.5M Na_2WO_4 (Na^+ has 4 molecules in its first solvation shell; WO_4 has got 12³⁷), a similar value than for a 5M NaCl solution. A classical view of the nucleation of stretched solution is to assume that the surface tension is increased due to the abundance of bound water molecules in the solution, enhancing the nucleation barrier⁸. The present contribution outlines another angle of view, by considering a diminished tension in the first hydration shells throughout the solution which decreases the thermodynamic driving force towards nucleation.

On another point of view, the present work exemplifies the ability of tension to be transmitted all around a stretched material, illustrating the realm of the tensile world. Water molecules under tension are able to pull on other materials than sister water molecules. As a consequence, a stretched solvent not only retains modified thermodynamic properties, but also modifies those of the matter with which it is interacting, like solutes, suspended particles, or (organic or inorganic) solids.

One practical consequence afforded in this paper, is that the chemical potential of solutes having negative volumes are lower than those expected from solutes at the same tension than the water solvent. As a result, the solubility effect of superheated liquids is enforced and their super-solvent feature still improved. This picture is complexified by the fact that some solutes have positive apparent volumes, and therefore should display the opposite trend, with a solubility decreasing with water tension. It is also diversified by considering that each type of solutes exert a specific damping effect related to its solvation features. Yet, this changing solubility is ultimately linked to the solvation thermodynamics which may become more or less favourable with the mechanical stretching on the solvation shells, making less/more costly to maintain hydrated solutes. Also, the damping effect which makes up the thermodynamic properties of the solutes comes into play with other, possibly kinetic, parameters, to build macroscopic complex behaviors. Eventually, the solubility picture that emerges from this study appears much more subtle and varied than usually considered.

ACKNOWLEDGMENTS

This work has received support from the French Agency for Research (Agence Nationale de la Recherche, ANR) through the grant CONGE BLAN-610-01, the Equipex Planex ANR-11-EQPX-36 and the Labex Voltaire ANR-10-LABX-100-01. Jean-Louis Hazemann is greatly acknowledged for his support for the calibration done at the Néel Institute in Grenoble. We are indebted to two anonymous referees who greatly helped us to improve the initial manuscript.

REFERENCES

- (1) Imre, A.; Martinas, K.; Rebelo, L.P.N. Thermodynamics of Negative Pressures in Liquids. *J. Non-Equilib. Thermodyn.* **1998**, *23*, 351-375.
- (2) Mercury, L.; Tardy, Y. Negative Pressure of Stretched Liquid Water. Geochemistry of Soil Capillaries. *Geochim.Cosmochim. Acta* **2001**, *65*, 3391-3408.
- (3) Mercury, L.; Azaroual, M.; Zeyen, H.; Tardy, Y. Thermodynamic Properties of Solutions in Metastable Systems under Negative or Positive Pressures. *Geochim. Cosmochim. Acta* **2003**, *67*, 1769-1785.
- (4) Lassin, A.; Marty, N.; Henry, B.; Trémosa, J.; Gailhanou, H.; Madé, B.; Altmann, S.; Gaucher, E.C. Equilibrium Partial Pressure of CO₂ in the Callovo-Oxfordian Argillite as a Function of Relative Humidity. *Procedia Earth Planet. Sci.* **2013**, *7*, 459-462.
- (5) Bouzid, M.; Mercury, L.; Lassin, A.; Matray, J.-M.; Azaroual, M. In-pore Tensile Stress by Drying-Induced Capillary Bridges Inside Porous Materials. *J. Colloid Interf. Sci.* **2011**, *355*, 498-506.
- (6) Bouzid, M.; Mercury, L.; Lassin, A.; Matray, J.-M.; Azaroual, M. Salt Precipitation and Trapped Liquid Cavitation in Micrometric Capillary Tubes. *J. Colloid Interf. Sci.* **2011**, *360*, 768-776.
- (7) Tarantola, A.; Caumon, M.-C. Raman Spectra of Water in Fluid Inclusions: II. Effect of Negative Pressure on Salinity Measurement. *J. Raman Spectrosc.* **2015**, *46*, 977-982.

- (8) Shmulovich, K.I.; Mercury, L.; Thiéry, R.; Ramboz, C.; El Mekki, M. Experimental Superheating of Water and Aqueous Solutions. *Geochim. Cosmochim. Acta* **2009**, *73*, 2457-2470.
- (9) Thiéry, R.; Mercury, L. Explosive Properties of Water in Volcanic and Hydrothermal Systems. *J. Geophys. Res.* **2009**, *114*, B05205, 1-19.
- (10) Thiéry, R.; Mercury, L. Explosivity Conditions of Aqueous Solutions. *J. Sol. Chem.* **2009**, *38*, 893–905.
- (11) Chienthavorn, O.; Su-in, P. Modified Superheated Water Extraction of Pesticides from Spiked Sediment and Soil. *Anal. Bioanal. Chem.* **2006**, *385*, 83-89.
- (12) Smith, R.M. Extractions with superheated water. *J. Chromatogr. A* **2002**, *975*, 31-46.
Smith, R.M. Superheated Water: the Ultimate Green Solvent for Separation Science. *Anal. Bioanal. Chem.* **2006**, *385*, 419-421.
- (13) Pettenati, M.; Mercury, L.; Azaroual, M. Capillary Geochemistry in Non-Saturated Zone of Soils. Water Content and Geochemical Signatures. *Applied Geochem.* **2008**, *23*, 3799-3818.
- (14) Roedder, E. Metastable Superheated Ice in Liquid-Water Inclusions under High Negative Pressure. *Science* **1967**, *155*, 1413-1417.
- (15) Green, J.L.; Durben, D.J.; Wolf, G.H.; Angell, C.A. Water and Solutions at Negative Pressure: Raman Spectroscopic Study to –80 Megapascals. *Science* **1990**, *249*, 649–652.
- (16) Zheng, Q.; Durben, D.J.; Wolf, G.H.; Angell, C.A. Liquids at Large Negative Pressures: Water at the Homogeneous Nucleation Limit. *Science* **1991**, *254*, 829-832.
- (17) Alvarenga, A.D.; Grimsditch, M.; Bodnar, R.J. Elastic Properties of Water under Negative Pressures. *J. Chem. Phys.* **1993**, *98*, 8392-8396.
- (18) Shmulovich, K.I.; Gorbaty, Yu.E.; Bondarenko, G.V. Pressure Dependence of the Raman Spectra of Aqueous Solutions and Anthracene. *Russ. J. Phys. Chem. B* **2012**, *6*, 907–911.

- (19) Shmulovich, K.I.; Yardley, B.W.D.; Graham, C.M. Solubility of Quartz in Crustal Fluids: Experiments and General Equations for Salt Solutions and H₂O–CO₂ Mixtures at 400–800°C and 0.1–0.9 GPa. *Geofluids* **2006**, *6*, 157-167.
- (20) In *Handbook of Chemistry and Physics* (Ed. D.R. Lide), 87th edition, CRC Press, Boca Raton, **2006**, pp. A-91.
- (21) Diamond, L.W. Chapter 3. Systematics of H₂O inclusions. In *Fluid inclusions, Analysis and Interpretation* (Eds Samson, I.; Anderson, A.; Marschall, D.), Mineralogical Association of Canada, **2003**, *32*, 55-79.
- (22) Mercury, L.; Jamme, F.; Dumas, P. Infrared Imaging of Bulk Water and Water-Solid Interfaces under Stable and Metastable Conditions. *Phys. Chem. Chem. Phys.* **2012**, *14*, 2864-2874.
- (23) Takahashi, M.; Izawa, E.; Etou, J.; Ohtani, T. Kinetic Characteristic of Bubble Nucleation in Superheated Water Using Fluid Inclusions. *J. Phys. Soc. Japan* **2002**, *71*, 2174-2177.
- (24) El Mekki, M.; Ramboz, C.; Perdereau, L.; Shmulovich, K.I.; Mercury, L. Lifetime of Superheated Water in a Micrometric Fluid Inclusion. In *Metastable Systems under Pressure*, NATO Science for Peace and Security Series A (Eds Rzoska, S.J.; Drozd-Rzoska, A.; Mazur, V.), Springer Verlag, **2010**, 279-292.
- (25) Guimbretière, G.; Canizarès, A.; Raimboux, N.; Joseph, J.; Desgardin, P.; Desgranges, L.; Jegou, C.; Simon, P. High Temperature Raman Study of UO₂: A Possible Tool for in situ Estimation of Irradiation-Induced Heating. *J. Raman Spectrosc.* **2015**, *46*, 418-420.
- (26) Testemale, D.; Argoud, R.; Geaymond, O.; Hazemann, J.-L. High Pressure/High Temperature Cell for X-Ray Absorption and Scattering Techniques. *Rev. Sci. Instrum.*, **2005**, *76*, 043905, 1-5.
- (27) Gregora, I.; Magneron, N.; Simon, P.; Luspín, Y.; Raimboux, N.; Philippot, E. Raman Study of AlPO₄ Berlinite at the Alpha-Beta Transition. *J. Phys. Condens. Matter* **2003**, *15*, 4487-4501.

- (28) Zhang, Y.-G.; Frantz, J. Determination of the Homogenization Temperatures and Densities of Supercritical Fluids in the System NaCl–KCl–CaCl₂–H₂O Synthetic Fluid Inclusions. *Chem. Geol.* **1987**, *64*, 335-350.
- (29) Mao, S.D.; Duan, Z.H. The PVTX Properties of Binary Aqueous Chloride Solutions up to T = 573 K and 100 MPa. *J. Chem. Therm.* **2008**, *40*, 1046-1063.
- (30) Dean, K.J.; Wilkinson, G.R. Precision Raman Investigation of the ν_1 Mode of Vibration of SO₄²⁻, WO₄²⁻ and MoO₄²⁻ in Aqueous Solutions of Different Concentrations *J. Raman Spectrosc.*, **1983**, *14*, 130-134.
- (31) Davitt, K.; Rolley, E.; Caupin, F.; Arvengas, A.; Balibar, S. Equation of State of Water under Negative Pressure. *J. Chem. Phys.* **2010**, *133*, 174507, 1-8.
- (32) Span, R.; Wagner, W. On the Extrapolation Behavior of Empirical Equation of State. *Int. J. Thermophys.* **1997**, *18*, 1415-1443.
- (33) Bodnar, R. J. Chapter 4. Introduction to Aqueous-Electrolyte Fluid Inclusions. In *Fluid Inclusions. Analysis and Interpretation* (Eds Samson, I.; Anderson, A.; Marschall, D.), Mineralogical Association of Canada, **2003**, *32*, 80-100.
- (34) Danielewicz-Ferchmin, I. The Ion Hydration Shell: Electrostatic and Thermodynamic Approach. *J. Phys. Chem.*, **1990**, *94*, 4335-4337.
- (35) Danielewicz-Ferchmin, I. Phase Diagram of Hydration Shells in Ionic Solutions *J. Phys. Chem.*, **1995**, *99*, 5658-5665.
- (36) Danielewicz-Ferchmin, I.; Ferchmin, A.R. Mass density in Hydration Shells of Ions. *Physica B* **1998**, *245*, 34-44.
- (37) Ohtaki, H.; Radnai, T. Structure and Dynamics of Hydrated Ions. *Chem. Rev.*, **1993**, *93*, 1157-1204.
- (38) Tanger IV, J.C.; Helgeson, H.C. Calculation of the Thermodynamic and Transport Properties of Aqueous Species at High Pressures and Temperatures: Revised Equations of State for the Standard Partial Molal Properties of Ions and Electrolytes. *Am. J. Sc.* **1988**, *288*, 19-98.

(39) Shock, E.L.; Helgeson, H.C.; Sverjensky, D.A. Calculations of the Thermodynamic and Transport Properties of Aqueous Species at High Pressures and Temperatures: Standard Partial Molal Properties of Inorganic Neutral Species. *Geochim. Cosmochim. Acta* **1989**, *53*, 2157-2183.

Table of Contents Graphic

